Accurate and efficient treatment of spin-orbit coupling via second variation employing local orbitals

Cecilia Vona,[1,*,†] Sven Lubeck,[1,*] Hannah Kleine,[1] Andris Gulans,[2] and Claudia Draxl[1,3]
[1]*Institut für Physik and IRIS Adlershof, Humboldt-Universität zu Berlin, 12489 Berlin, Germany*
[2]*Department of Physics, University of Latvia, 1004 Riga, Latvia*
[3]*European Theoretical Spectroscopic Facility (ETSF)*

(Received 18 June 2023; revised 8 November 2023; accepted 20 November 2023; published 20 December 2023)

A method is presented that allows for efficient evaluation of spin-orbit coupling (SOC) in density-functional-theory calculations. In the so-called second-variational scheme, where Kohn-Sham functions obtained in a scalar-relativistic calculation are employed as a basis for the spin-orbit-coupled problem, we introduce a rich set of local orbitals as additional basis functions. Also, relativistic local orbitals can be used. The method is implemented in the all-electron full-potential code EXCITING. We show that, for materials with strong SOC effects, this approach can reduce the overall basis-set size and thus computational costs tremendously.

DOI: 10.1103/PhysRevB.108.235161

I. INTRODUCTION

Spin-orbit coupling (SOC) is crucially important for accurate electronic-structure calculations of many materials. To illustrate, SOC is responsible for lifting the degeneracy of low-energy excitons in transition-metal dichalcogenides [1–3], opening a tiny gap in graphene [4–6], and dramatically lowering the fundamental band gap in halide perovskites [7]. However, the impact of SOC is not limited to changing the features of electronic bands. It affects bond lengths [8–10] and phonon energies [8,11] and even turns deep defects into shallow ones [12].

In density-functional-theory (DFT) computations, SOC is treated differently in the various methods and codes. Major differences occur in the treatment of the four-component Dirac equation, for which several levels of approximations exist, and in the basis functions used for expanding the Kohn-Sham wave functions [13–19]. In the context of the numerical representation, the family of full-potential linearized augmented plane wave (LAPW) methods is commonly used as a reference, e.g., for new implementations [15] and for assessing pseudopotentials [20]. LAPW codes [21–24] typically follow a common strategy to account for relativistic effects, including SOC. For low-lying core orbitals, the standard approach is to solve the radial four-component Dirac equation, assuming a spherically symmetric potential. For the semicore and valence electrons, the common strategy is a two-step procedure [25] referred to as SR+SOC. First, the Kohn-Sham (KS) problem is solved within the scalar-relativistic (SR) approximation [first variation (FV)]. For this purpose, typically, either the Koelling-Harmon approach [26] or the zero-order approximation (ZORA) [27,28] is employed. Then, the solutions of the full problem including SOC are constructed using the FV wave functions as the basis. This step is known as the second variation (SV). The strategy relies on the assumption that SOC introduces a small perturbation, and indeed, this scheme is appropriate and efficient for many materials since all the occupied and only a handful of unoccupied bands are often sufficient. Under these circumstances, the two-step procedure offers a clear computational advantage over methods in which SOC is treated on the same footing as other terms of the Hamiltonian [10,29,30].

Some materials, however, require more involved calculations than others. For example, it was argued by Scheidemantel and coworkers [31] that Bi_2Te_3 requires the consideration of unoccupied bands of at least 8 Ry above the Fermi level to give reliable results. Even more striking, in halide perovskites, the full set of KS orbitals is needed for convergence [32]. These cases illustrate that, as already argued [33], for some materials, the SV approach fails to achieve the expected efficiency and SOC cannot be considered a small perturbation. Moreover, it is known that scalar- and fully relativistic orbitals have different asymptotic behaviors at small distances from the nuclei, which cannot be recovered in terms of scalar-relativistic functions. Therefore, in Refs. [25,34], the SV basis was extended by additional basis functions, local orbitals (LOs), that recover the correct asymptotic behavior of the $p_{1/2}$ orbitals. This approach is a step forward compared to conventional SV calculations. However, by introducing only $p_{1/2}$ LOs, this method does not offer the possibility of systematic improvement toward the complete-basis-set limit. There are examples of SR calculations in the literature in which an extensive use of LOs is required to reach precision targets [35–37]. Furthermore, Ref. [30] demonstrated this point also in the context of fully relativistic calculations. We therefore conclude that the state-of-the-art SV approaches, be it with or without $p_{1/2}$ LOs, are not sufficient for a systematic description of SOC in condensed-matter systems.

In this work, we introduce a numerical approach termed *second variation with local orbitals* (SVLO) which makes use of the fact that relativistic effects are strongest around the atomic nuclei. Therefore, in comparison to the standard SV

*These authors contributed equally to this work.
†Corresponding author: cecilia.vona@physik.hu-berlin.de

approach, it is important to increase the flexibility of the basis specifically in these regions. To satisfy this need, we express the solution of the full problem in terms of FV wave functions and rich sets of LOs. In contrast to the usual approach, all LOs are treated as explicit basis functions also on the SV level. Moreover, aiming at a highly precise evaluation of SOC, we extend the SVLO method by adding LOs beyond $p_{1/2}$ functions. They are obtained by solving the radial Dirac equation, and we refer to them as Dirac-type LOs below. Based on the implementation in the all-electron full-potential package EXCITING [21], we demonstrate and validate our method using band-structure and total-energy calculations of Xe, MoS_2, PbI_2, γ-$CsPbI_3$, and Bi_2Te_3.

II. METHOD

A. Conventional second variation in the LAPW+LO framework

We consider the two-component KS equations

$$\sum_{\sigma'=\uparrow,\downarrow} \hat{H}_{\sigma\sigma'}\Psi_{n\boldsymbol{k}\sigma'}(\boldsymbol{r}) = \varepsilon_{n\boldsymbol{k}}\Psi_{n\boldsymbol{k}\sigma}(\boldsymbol{r}) \tag{1}$$

for the spin components $\sigma = \uparrow, \downarrow$. The resulting single-particle spinors $\Psi_{n\boldsymbol{k}}(\boldsymbol{r}) = \sum_\sigma \Psi_{n\boldsymbol{k}\sigma}(\boldsymbol{r})|\sigma\rangle$ ($|\sigma\rangle$ is the spin state) have eigenenergies $\varepsilon_{n\boldsymbol{k}}$, where n is the band index and $\boldsymbol{k}$ is the Bloch wave vector. The Hamiltonian $\hat{H}_{\sigma\sigma'}$ consists of a SR part and a spin-orbit part that couples the two spin components:

$$\hat{H}_{\sigma\sigma'} = \delta_{\sigma\sigma'}\hat{H}^{\mathrm{SR}}_{\sigma} + \hat{H}^{\mathrm{SOC}}_{\sigma\sigma'}. \tag{2}$$

As described in Refs. [10,29,30], Eq. (1) can be solved directly, i.e., nonperturbatively, requiring a significantly larger computational effort compared to a SR calculation. Given that $\hat{H}^{\mathrm{SOC}}_{\sigma\sigma'}$ typically leads to a small correction, it is not efficient to pay the full price for the nonperturbative (NP) solution, and thus, the conventional SV method is often employed. Here, first, one solves the SR problem in the FV,

$$\hat{H}^{\mathrm{SR}}_{\sigma}\Psi^{\mathrm{FV}}_{j\boldsymbol{k}\sigma}(\boldsymbol{r}) = \varepsilon^{\mathrm{FV}}_{j\boldsymbol{k}\sigma}\Psi^{\mathrm{FV}}_{j\boldsymbol{k}\sigma}(\boldsymbol{r}). \tag{3}$$

Within the LAPW+LO method, this is achieved by solving the matrix equation that is obtained by expanding the FV KS wave functions $\Psi^{\mathrm{FV}}_{j\boldsymbol{k}\sigma}(\boldsymbol{r})$ in terms of two distinct types of basis functions, namely, LAPWs $\phi_{\boldsymbol{G}\boldsymbol{k}}(\boldsymbol{r})$ and LOs $\phi_\mu(\boldsymbol{r})$, which are indexed by the reciprocal lattice vector $\boldsymbol{G}$ and LO index μ, respectively,

$$\Psi^{\mathrm{FV}}_{j\boldsymbol{k}\sigma}(\boldsymbol{r}) = \sum_{\boldsymbol{G}} C_{\boldsymbol{k}\sigma\boldsymbol{G}j}\phi_{\boldsymbol{G}\boldsymbol{k}}(\boldsymbol{r}) + \sum_{\mu} C_{\boldsymbol{k}\sigma\mu j}\phi_\mu(\boldsymbol{r}). \tag{4}$$

Second, one uses the resulting FV eigenstates as a basis for the SV eigenstates,

$$\Psi^{\mathrm{SV}}_{n\boldsymbol{k}}(\boldsymbol{r}) = \sum_{\sigma j} C^{\mathrm{SV}}_{\boldsymbol{k}\sigma jn}\Psi^{\mathrm{FV}}_{j\boldsymbol{k}\sigma}(\boldsymbol{r})|\sigma\rangle. \tag{5}$$

Here, j runs over all occupied (N_{occ}) and a limited number of unoccupied (N_{unocc}) FV KS states. Approximating the exact solution $\Psi_{n\boldsymbol{k}}(\boldsymbol{r})$ by $\Psi^{\mathrm{SV}}_{n\boldsymbol{k}}(\boldsymbol{r})$, one obtains the SV eigenequation for the expansion coefficients $C^{\mathrm{SV}}_{\boldsymbol{k}\sigma jn}$,

$$\sum_{\sigma' j'} H_{\boldsymbol{k}\sigma\sigma' jj'}C^{\mathrm{SV}}_{\boldsymbol{k}\sigma' j'n} = \varepsilon^{\mathrm{SV}}_{n\boldsymbol{k}}C^{\mathrm{SV}}_{\boldsymbol{k}\sigma jn}, \tag{6}$$

where $H_{\boldsymbol{k}\sigma\sigma' jj'}$ are the matrix elements of $\hat{H}_{\sigma\sigma'}$, as defined in Eq. (2), with respect to the basis functions $\Psi^{\mathrm{FV}}_{j\boldsymbol{k}\sigma}(\boldsymbol{r})$,

$$\begin{aligned} H_{\boldsymbol{k}\sigma\sigma' jj'} &= \left\langle \Psi^{\mathrm{FV}}_{j\boldsymbol{k}\sigma}\middle|\hat{H}_{\sigma\sigma'}\middle|\Psi^{\mathrm{FV}}_{j'\boldsymbol{k}\sigma'}\right\rangle \\ &= \delta_{\sigma\sigma'}\delta_{jj'}\varepsilon^{\mathrm{FV}}_{j\boldsymbol{k}\sigma} + \left\langle \Psi^{\mathrm{FV}}_{j\boldsymbol{k}\sigma}\middle|\hat{H}^{\mathrm{SOC}}_{\sigma\sigma'}\middle|\Psi^{\mathrm{FV}}_{j'\boldsymbol{k}\sigma'}\right\rangle. \end{aligned} \tag{7}$$

B. Second variation with local orbitals as explicit basis functions

The SVLO approach is a modification of the conventional second variation. It preserves the solution of the FV problem by using the LAPW+LO basis of Eq. (4) to solve Eq. (3). We then exploit the duality of the basis and add the same set of LOs as explicit basis functions to the set of FV eigenfunctions to solve the SV problem. To avoid linear-dependence problems between these two sets, we modify the FV eigenfunctions so that the LO contributions are neglected and only the first sum in Eq. (4) is further considered:

$$\bar{\Psi}^{\mathrm{FV}}_{j\boldsymbol{k}\sigma}(\boldsymbol{r}) = \sum_{\boldsymbol{G}} C_{\boldsymbol{k}\sigma\boldsymbol{G}j}\phi_{\boldsymbol{G}\boldsymbol{k}}(\boldsymbol{r}). \tag{8}$$

We combine these modified FV functions with the original set of LOs to form the SVLO basis

$$\Psi^{\mathrm{SVLO}}_{n\boldsymbol{k}}(\boldsymbol{r}) = \sum_{\sigma j} C^{\mathrm{SVLO}}_{\boldsymbol{k}\sigma jn}\bar{\Psi}^{\mathrm{FV}}_{j\boldsymbol{k}\sigma}(\boldsymbol{r})|\sigma\rangle + \sum_{\sigma\mu} C^{\mathrm{SVLO}}_{\boldsymbol{k}\sigma\mu n}\phi_\mu(\boldsymbol{r})|\sigma\rangle. \tag{9}$$

The total basis-set size then includes the number of these LO basis functions N_{LO}. To summarize, the total number of basis functions in the two methods is

$$N_{\mathrm{b}}^{\mathrm{SV(LO)}} = \begin{cases} N_{\mathrm{occ}} + N_{\mathrm{unocc}} & \mathrm{SV} \\ N_{\mathrm{occ}} + N_{\mathrm{unocc}} + N_{\mathrm{LO}} & \mathrm{SVLO}. \end{cases} \tag{10}$$

In both cases, N_{unocc} is a computational parameter, and the results need to be converged with respect to it. We note in passing that the SVLO basis is not orthogonal and thus carries a slight computational overhead compared to the conventional SV method since it leads to a generalized eigenvalue problem.

The SVLO method is implemented in EXCITING. How the different types of LOs are constructed will be described in the next section. Unlike Refs. [25,34], our approach uses the entire set of LOs from the FV basis (including Dirac-type LOs if necessary) as the basis in the SV step.

C. Dirac-type local orbitals

LOs are basis functions with the characteristic of being nonzero only in a sphere centered at a specific nucleus α [38]. They take the form of atomiclike orbitals, which read

$$\phi_\mu(\boldsymbol{r}) = \delta_{\alpha,\alpha_\mu}\delta_{l,l_\mu}\delta_{m,m_\mu}U_\mu(r_\alpha)Y_{lm}(\hat{r}_\alpha), \tag{11}$$

where $Y_{lm}(\hat{r}_\alpha)$ are spherical harmonics and $U_\mu(r_\alpha)$ are linear combinations of two or more radial functions. In the SR case, this reads

$$U^{\mathrm{SR}}_\mu(r_\alpha) = \sum_\xi a_{\mu\xi}u_{\alpha\xi l}(r_\alpha;\varepsilon_{\alpha\xi l}). \tag{12}$$

The radial functions $u_{\alpha\xi l}$ are solutions of the SR Schrödinger equation, evaluated at predefined energy parameters $\varepsilon_{\alpha\xi l}$. Note that the sum over ξ could also include their energy derivatives

TABLE I. Structural information and convergence parameters used in the calculations for the considered materials. $R_{\mathrm{MT}}^{\mathrm{min}}G_{\mathrm{max}}$ is the product of the largest reciprocal lattice vector G_{max} considered in the LAPW basis and the (smallest) MT radius $R_{\mathrm{MT}}^{\mathrm{min}}$. For MoS_2, the latter refers to the S sphere ($R_{\mathrm{MT}} = 2.05a_0$). For more detailed information, we refer to the input files provided at NOMAD [41].

	Material				
	Xe	MoS_2	PbI_2	$CsPbI_3$	Bi_2Te_3
Space group	$Fm3$-m	P-$6m2$	P-$3m1$	$Pnma$	R-$3m$
a (Å)	6.20	3.16	4.56	8.86	10.44
b (Å)	6.20	3.16	4.56	8.57	10.44
c (Å)	6.20	15.88	6.99	12.47	10.44
Ref.	[42,43]	[44]	[45]	[46]	[47]
R_{MT} (in units of a_0)	3.00	2.30/2.05	2.90	2.90	2.80
$R_{\mathrm{MT}}^{\mathrm{min}}G_{\mathrm{max}}$	8	8	8	9	10
$\boldsymbol{k}$ mesh	$4 \times 4 \times 4$	$6 \times 6 \times 1$	$6 \times 6 \times 4$	$3 \times 3 \times 2$	$6 \times 6 \times 6$

of any order (for brevity not explicitly written here). Depending on their purpose, all radial functions may be evaluated either with the same energy parameter or with one corresponding to a different state. The Dirac-type LOs differ only in the type of radial functions used in the sum,

$$U_{\mu}^{\mathrm{Dirac}}(r_\alpha) = \sum_{\xi} a_{\mu\xi} u_{\alpha\xi lJ}(r_\alpha; \varepsilon_{\alpha\xi lJ}), \tag{13}$$

where $u_{\alpha\xi lJ}$ are solutions of the radial Dirac equation. They account for the proper asymptotic behavior of the basis at the atomic nuclei. The energy parameters are also characterized by the total angular momentum J. In our implementation, it is possible to combine radial functions with different total angular momenta (but the same angular momentum l). It is also possible to combine J-resolved radial functions with SR radial functions. In the following, we call any LOs including at least one J-resolved radial function Dirac-type LOs. With this, we can add one or more LOs with any relativistic quantum number, going beyond adding only $p_{1/2}$ LOs as suggested by Singh [25] and applied by Kuneš and coworkers [34]. This approach, also used in Ref. [10], preserves the characteristic behavior of the LO near the nucleus while being more convenient than other methods, such as the fully relativistic augmented plane-wave basis proposed in Ref. [29]. In the latter, the basis functions consist of the full solution of the radial Dirac equation combined with spin harmonics, while here, the general form of the LOs in Eq. (11) is kept in terms of spherical harmonics, and only the radial functions are modified.

III. COMPUTATIONAL DETAILS

We consider a set of five materials, including three-dimensional and two-dimensional (2D) semiconductors and a topological insulator, with different atomic species, stoichiometries, and degrees of SOC. For all of them, we use the experimentally determined lattice constants and atomic positions. All calculations are performed with the package EXCITING [21], in which our method is implemented. Exchange and correlation effects are treated by the Perdew-Burke-Ernzerhof parametrization [39,40] of the generalized gradient approximation. Core electrons are described by means of the four-component Dirac equation, while valence/semicore states are treated scalar relativistically using ZORA. The SOC term is applied only within the muffin-tin (MT) region and is evaluated self-consistently using the following expression:

$$\hat{H}^{\mathrm{SOC}} = \frac{c^2}{(2c^2 - V)^2} \frac{1}{r} \frac{dV}{dr} \boldsymbol{\sigma} \boldsymbol{L}, \tag{14}$$

where $\boldsymbol{\sigma}$ and V are the vector of Pauli matrices and the spherically symmetric component of the KS potential, respectively, and c is the speed of light.

The structural and computational parameters are displayed in Table I. The respective $\boldsymbol{k}$ mesh and the dimensionless LAPW cutoff $R_{\mathrm{MT}}^{\mathrm{min}}G_{\mathrm{max}}$ are chosen such that total energies per atom and band gaps are within a numerical precision of 10^{-2} eV/atom and 10^{-2} eV, respectively. The actual LAPW basis cutoff G_{max} is determined by dividing $R_{\mathrm{MT}}^{\mathrm{min}}G_{\mathrm{max}}$ by the smallest MT radius $R_{\mathrm{MT}}^{\mathrm{min}}$ of the considered system.

SR calculations are used for comparison with the other methods to investigate the magnitude of SOC effects. To determine the advantages of the SVLO over the SV method, we carefully monitored the convergence of all considered quantities with respect to the number of SV(LO) basis functions. The NP method, as described in Ref. [10], is used as a reference for this assessment.

For SR and SV calculations, we employ SR LOs. As we mainly address p states in our examples, we label this case p. The LO set including Dirac-type LOs, referred to as $p_{1/2}$, is constructed by adding to the SR LOs two $p_{1/2}$-type LOs for each p state. Due to their p character, each LO gives rise to three degenerate basis functions. The method is, however, fully general since it allows to include relativistic LOs of other characters. For instance, we explore the effect of $d_{3/2}$ LOs in MoS_2 since its valence band maximum (VBM) and conduction band minimum (CBM) exhibit a predominant d character [48]. As the impact on the total energy and the electronic structure turns out to be negligible, however, we do not include this case in the following analysis. In the other materials, we additionally investigate the effects of $p_{3/2}$ LOs by replacing the p LOs. Due to their similar behavior near the nuclei, their impact is, however, only of the order of 10^{-2} eV or smaller, which is within our convergence criteria. For this reason, we do not consider them further. $p_{1/2}$ LOs are used in SVLO and in the corresponding NP reference when specified. The number of LOs used in the different systems

TABLE II. Basis functions considered in the calculations of the five studied systems. N_{LAPW} is the number of LAPWs; N_{LO} ($N_{\mathrm{LO}}^{1/2}$) is the number of LO basis functions for calculations without (with) Dirac-type LOs. The last column shows the number of occupied valence states N_{occ}.

Material	N_{LAPW}	N_{LO}	$N_{\mathrm{LO}}^{1/2}$	N_{occ}
Xe	138	26	38	13
MoS_2	939	35		13
PbI_2	318	73	109	33
$CsPbI_3$	3236	496	736	228
Bi_2Te_3	895	141	201	57

is displayed in Table II together with the size of the LAPW basis and the number of occupied valence states. To obtain the band-gap position for Bi_2Te_3, for the different sets of LOs (p type and $p_{1/2}$ type), we perform, on top of the self-consistent NP calculation, an additional iteration with a $48 \times 48 \times 48$ $\boldsymbol{k}$ mesh. The so-determined respective $\boldsymbol{k}$ points are then included in the band-structure path, from which we extract the final values of the energy gaps in the SV and SVLO calculations.

IV. RESULTS

A. Xe

Our analysis starts with solid Xe. Figure 1 shows the convergence behavior of the total energy with respect to the number of basis functions, taking the NP calculation as a reference. For comparison, we also show the results of the conventional SV method. Since we employ the same number of occupied states in the SV and SVLO methods, for the p and $p_{1/2}$ sets of LOs (Table II), the number of basis functions on the x axis does not include the occupied states, i.e., $\tilde{N}_{\mathrm{b}}^{\mathrm{SV(LO)}} = N_{\mathrm{b}}^{\mathrm{SV(LO)}} - N_{\mathrm{occ}}$. $N_{\mathrm{b}}^{\mathrm{SV(LO)}}$ is defined in Eq. (10), which applies to both methods. The number of LO basis functions in the equation is also predetermined; therefore, the increase in $\tilde{N}_{\mathrm{b}}^{\mathrm{SV(LO)}}$ reflects only the number of unoccupied bands. We will always refer to $\tilde{N}_{\mathrm{b}}^{\mathrm{SV(LO)}}$ when discussing the basis-set size.

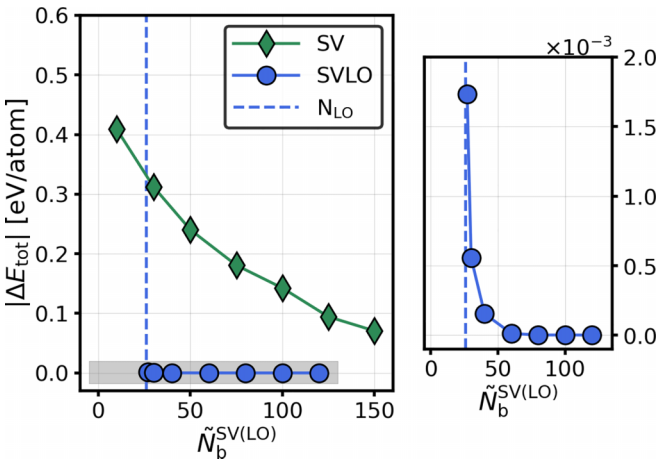

FIG. 1. Convergence behavior of the total energy with respect to the number of basis functions $\tilde{N}_{\mathrm{b}}^{\mathrm{SV(LO)}}$ (excluding occupied states). The energy of the NP calculation is taken as a reference. Blue circles indicate the SVLO scheme; green diamonds show the conventional SV treatment. The right panel zooms into the gray region where the SVLO method converges.

In the case of Xe, we consider 26 SR LO basis functions (see Table II).

Strikingly, the total-energy differences obtained by the SVLO method stay within 2×10^{-3} eV/atom when employing a total number of basis functions comparable to the number of LO basis functions, while the SV method requires all available FV states to reach values even one order of magnitude larger (7×10^{-2} eV/atom). To visualize this behavior better, Fig. 2 depicts the convergence of both methods on a logarithmic scale. We can observe that the SVLO method reaches convergence within 10^{-6} eV/atom with $\sim$80 basis functions. In Fig. 2, we also analyze the convergence of the energy gap E_{g} and the SOC splitting at the Γ point δ_{SOC}. When SOC is considered, E_{g} decreases by 0.43 eV due to the splitting of the (disregarding spin) threefold-degenerate VBM into a single state and a doubly degenerate state by about 1.30 eV (see also Table III and Fig. 3). For both E_{g} and δ_{SOC}, we observe that the SVLO method reaches a precision of the order of 10^{-4} eV already with a number of basis functions comparable to the number of LO functions; with approximately 80 basis functions it is even two orders of magnitude better. In contrast, the SV treatment, employing all available FV KS eigenstates, converges only within 10^{-3} and 10^{-2} eV for the energy gap and the SOC splitting, respectively. If we consider a target precision often used for production calculations such as 10^{-2} eV/atom for the total energy and 10^{-2} eV for energy gaps and SOC splittings, the advantage of the SVLO method is particularly considerable for the total energy. In contrast, the SV energy gap reaches the target precision at a number of empty states smaller than the number of LO basis functions, and the corresponding SOC splitting requires approximately 75 empty states.

Dirac-type LOs turn out to be significant for the SOC splitting, which increases by 0.1 eV (Table III) with the addition of four $p_{1/2}$-type LOs, each of them contributing three degenerate basis functions (Table II). Their effect on the energy gap is negligible. The convergence behavior of the energy gap and the SOC splitting with respect to the number of basis functions is comparable to that of the SVLO method with SR LOs (Fig. 2). Contrarily, the total energy converges to a worse precision (within 10^{-4} eV/atom). Also with Dirac-type LOs the analyzed quantities reach the targeted precision with a few empty states in addition to the LO basis functions. In the Appendix, we explain why the SV and SVLO methods do not converge to the same precision.

B. MoS_2

The transition-metal dichalcogenide MoS_2 is among the most studied 2D materials and a candidate for many applications in optoelectronics. SOC reduces the energy gap by only 0.07 eV (Table III), caused by a splitting of the VBM. Although this splitting is rather small, i.e., 0.15 eV, it is fundamental because not considering it could lead to the unphysical prediction of an indirect band gap [49]. Moreover, the splitting

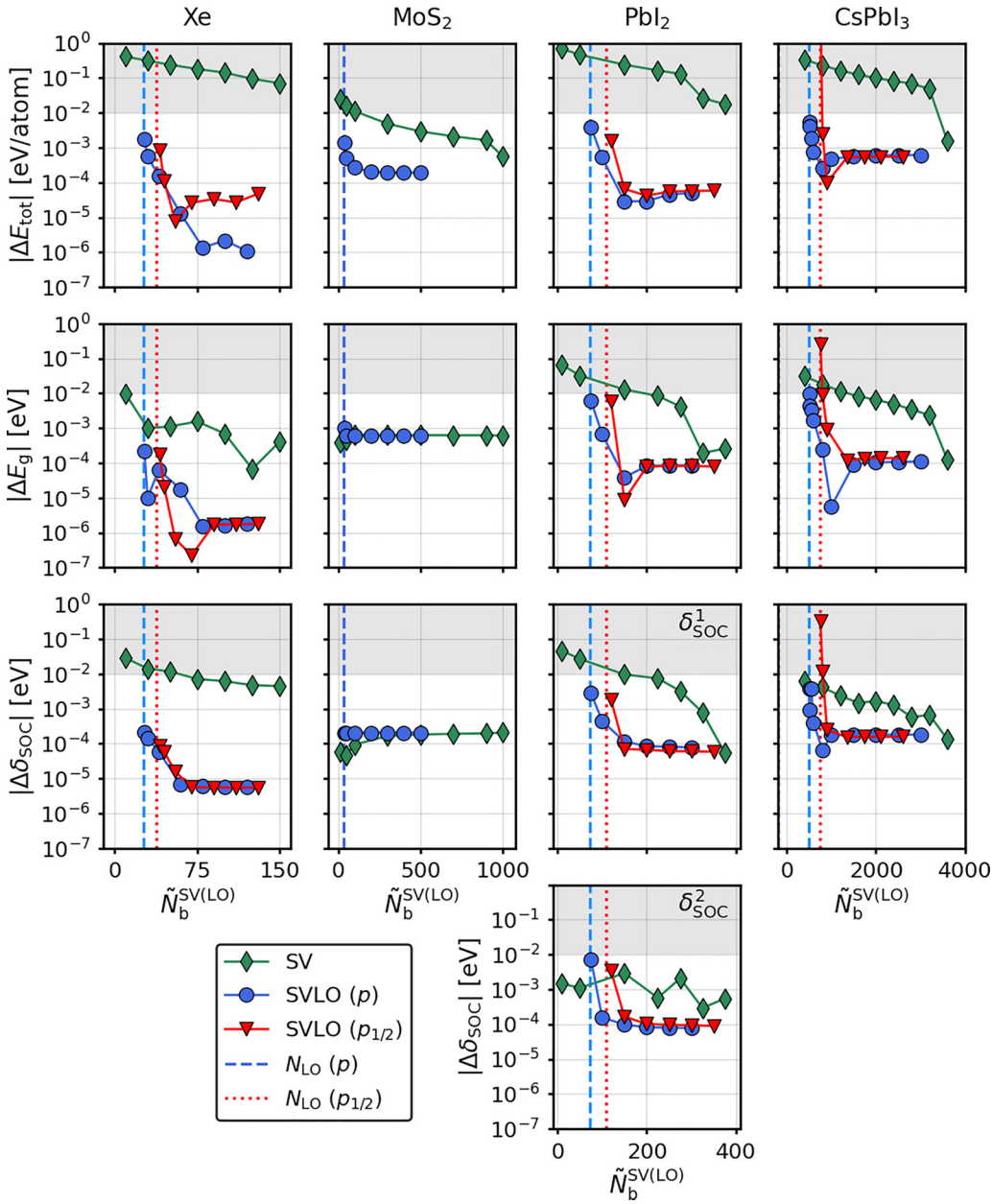

FIG. 2. Convergence behavior of the total energy, energy gap, and SOC splitting in Xe, MoS_2, PbI_2, and $CsPbI_3$, with respect to the number of basis functions used in the SV(LO) methods. Note the logarithmic scale on the y axes. For the energy differences, the NP results serve as a reference. In the NP reference calculations, we employ sets of p or $p_{1/2}$ LOs, depending on the method used for comparison. Green diamonds stand for the SV method with SR LOs. All other results are obtained with the SVLO method, using different types of LOs: those obtained using SR (Dirac-type) orbitals are indicated by blue circles (red triangles). The vertical lines mark the respective number of LO basis functions. For PbI_2, we display δ^2_{SOC} and the energy difference δ^1_{SOC} (both indicated in Fig. 3). The gray shaded areas are guides to the eye to highlight the points which are within the target precision (10^{-2} eV/atom for the total energy and 10^{-2} eV for the other quantities).

at the K point of the Brillouin zone (BZ) is essential for accurate description of the optical spectra [1,2]. Regarding the convergence behavior (second column of Fig. 2), we observe a small improvement of the SVLO method over the SV method for the total energy: With around 40 basis functions, the SVLO (SV) method reaches a precision of the order of 10^{-3} eV/atom (10^{-2} eV/atom). For the energy gap and the SOC splitting, both methods reach convergence with a few basis functions and reproduce the NP treatment with a precision of the order of 10^{-4} eV.

C. PbI_2

Lead iodide, PbI_2, is a semiconductor used for detectors, and it is also a precursor for the heavily investigated solar-cell materials lead-based halide perovskites. Like in the latter, in PbI_2, the SOC effects are massive. The band gap reduces by 0.54 eV (Table III and Fig. 3) and (disregarding spin) the twofold-degenerate second conduction band (CB) experiences a splitting of $\delta^2_{\mathrm{SOC}} = 0.63$ eV. There is also an increase in the energy distance between the CBM and the second CB of 0.31 eV (Table III). For convenience, we label this energy

TABLE III. Energy gaps E_g and SOC splittings δ_{SOC} of the considered materials computed with the SVLO method for different sets of LOs. For comparison, SR results are shown. For Bi_2Te_3, which does not exhibit any SOC splitting, we show the energy difference between the highest valence band and the lowest conduction band at Γ and $E_{\Gamma\to\Gamma}$. Note that in this material, SOC changes not only the magnitude of the gap but also the positions of the VBM and the CBM. Both are again altered when Dirac-type LOs are considered.

	E_g (eV)					δ_{SOC} (eV)					$E_{\Gamma\to\Gamma}$ (eV)
Method	Xe	MoS_2	PbI_2	$CsPbI_3$	Bi_2Te_3	Xe	MoS_2	PbI_2 (δ^1_{SOC})	PbI_2 (δ^2_{SOC})	$CsPbI_3$	Bi_2Te_3
SR	6.22	1.78	2.20	1.64	0.25 ($\Gamma\to\Gamma$)			0.94			0.25
SVLO (p)	5.79	1.71	1.66	0.82	0.10 ($B\to B$)	1.30	0.15	1.25	0.63	0.71	0.58
SVLO ($p_{1/2}$)	5.79		1.40	0.55	0.03 ($D\to C$)	1.40		1.45	0.68	0.76	0.69

difference as δ^1_{SOC}. For PbI_2, the advantages of the SVLO method over SV are considerable. With a number of basis functions comparable to the number of LO functions (here, 73; see Table II), the SVLO method reaches the target precision for all considered quantities (Fig. 2). Contrarily, the SV method requires basically all empty states (∼375 basis functions) to reach the target precision for the total energy; ∼225 empty bands are needed for the energy gap, and ∼150 are needed for δ^1_{SOC}, while only ∼10 empty states are needed for δ^2_{SOC}. Except for the total energy, for which the SV method converges to a precision of the order of 10^{-2} eV/atom and the SVLO method converges to a precision of the order of 10^{-5} eV/atom, both approaches converge to comparable precisions.

For an accurate prediction of the electronic structure, $p_{1/2}$-type LOs are crucial (Fig. 3). We add four for each species, with a total of 36 LOs basis functions (see Table II). They reduce the energy gap further by 0.26 eV and increase δ^1_{SOC} by an additional 0.20 eV. δ^2_{SOC} increases by only 0.05 eV (Table III). The convergence behavior with $p_{1/2}$-type LOs is, overall, comparable to that with SR LOs. Note that the two curves appear shifted by these 36 additional basis functions. Although this number of LO basis functions is considerable for such a system (see Table II), the speedup with respect to the SV method is significant also when Dirac-type LOs are employed.

D. $CsPbI_3$

$CsPbI_3$ is among the most studied inorganic metal halide perovskites [32,50]. We consider it in the orthorhombic γ phase that contains 20 atoms. Because it is composed of three

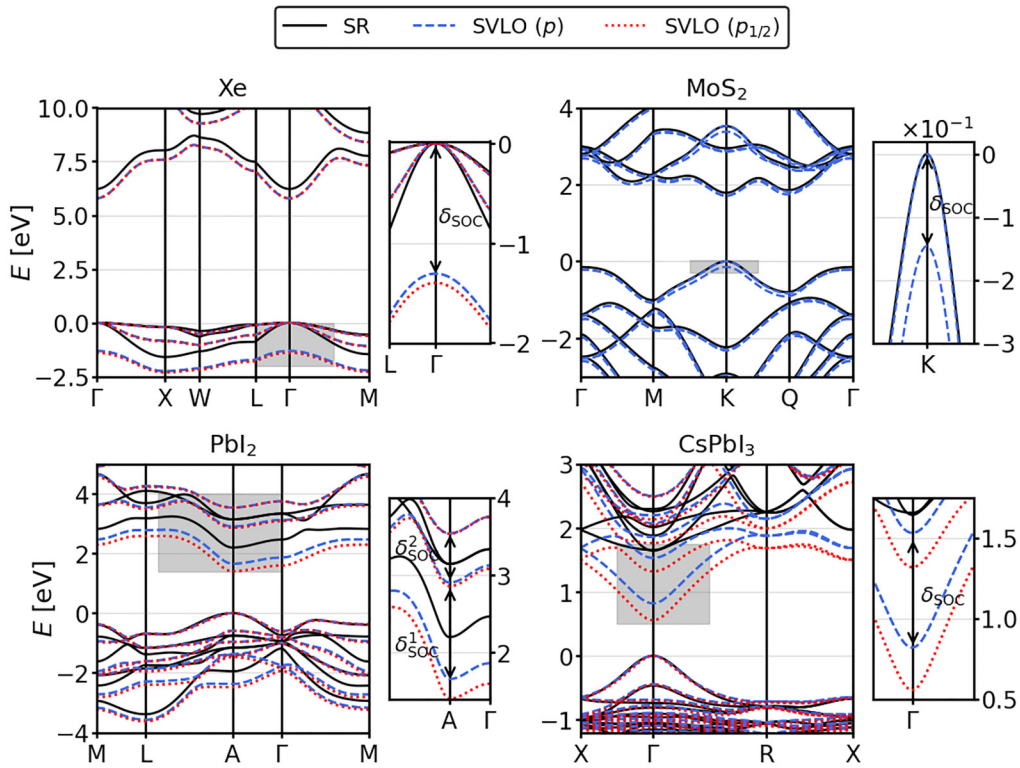

FIG. 3. Band structures of Xe (top left panel), Mo_2 (top right panel), PbI_2 (bottom left panel), and $CsPbI_3$ (bottom right panel) computed with different methods and types of local orbitals. Black lines correspond to SR calculations, and blue (red) lines correspond to the SVLO method without (with) Dirac-type orbitals. The VBM is set to zero. To the right of each panel, we zoom into the corresponding region indicated by the gray box.

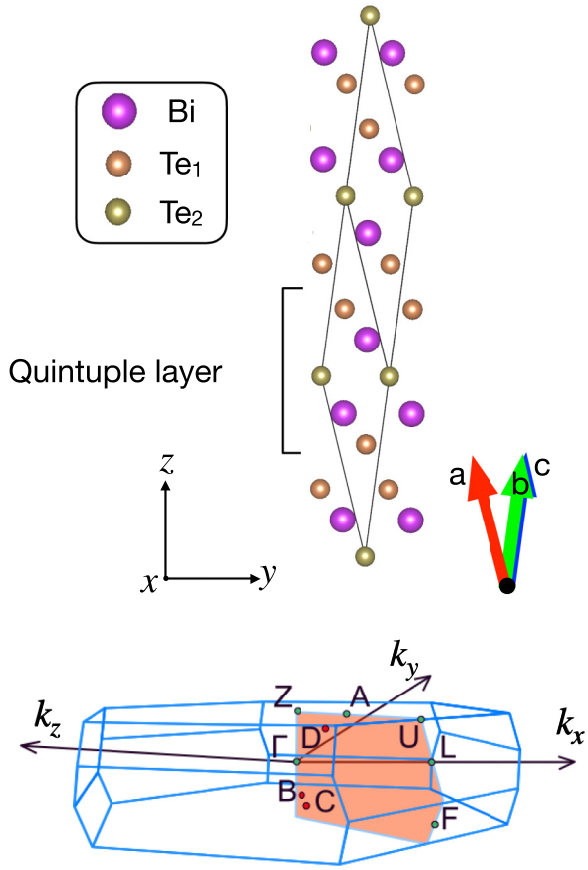

FIG. 4. Top: Crystal structure of Bi_2Te_3 built by Bi (purple) and two chemically inequivalent Te atoms (Te_1, orange; Te_2, gold). Bottom: Corresponding Brillouin zone. The mirror plane containing the points depicted in the band structure in Fig. 5 is indicated in red.

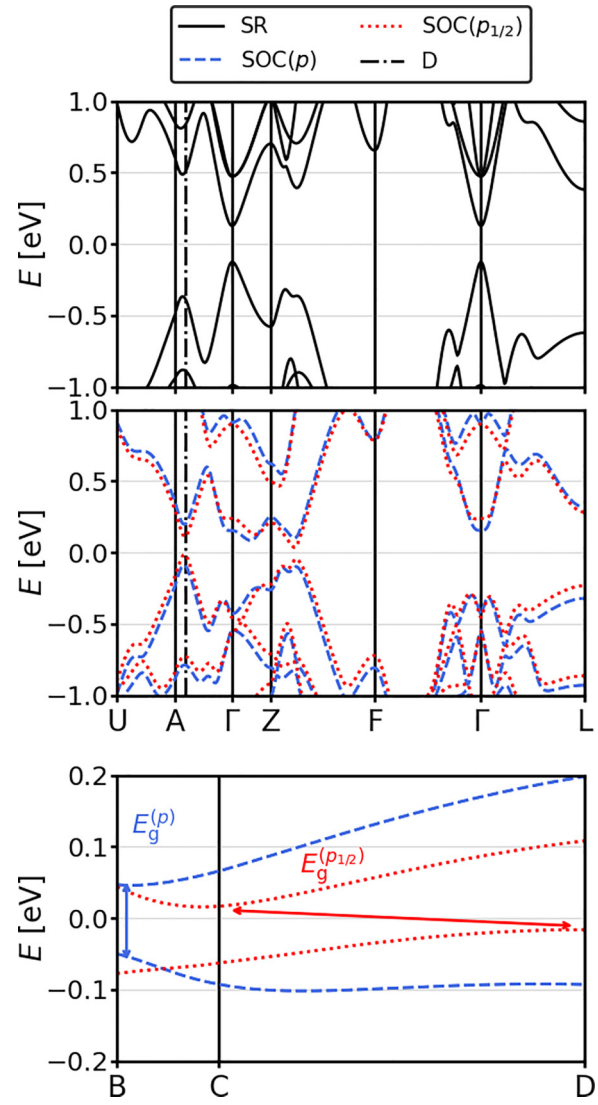

FIG. 5. Band structure of Bi_2Te_3, computed without (top panel) and with SOC (middle and bottom panels). The coordinates of the high-symmetry points are U, (0.823, 0.339, 0.339); Z, (0.5,0.5,0.5); F, (0.5,0.5,0.0); and L, (0.5,0.0,0.0); those of points A, B, C, and D are given in the text. The dashed vertical lines in the top and middle panels indicate the position of point D. The bottom panel zooms into the region of the band edges, showing the direct (indirect) band gap computed with p ($p_{1/2}$) LOs. Note that, different from Fig. 3, the energy zero is not at the VBM, but in the middle of the band gap.

heavy elements, SOC effects are enormous. The band gap decreases from 1.64 eV with SR to 0.82 eV when SOC is considered (Table III). This decrease is caused by a 0.71 eV splitting of the (disregarding spin) twofold-degenerate CBM (Fig. 3). When Dirac-type LOs are added, the gap further reduces by 0.27 eV, while the splitting increases by only 0.05 eV (Table III).

Although SV and SVLO(p) converge to the same results within the target precision, the computational effort required for the two approaches is noticeably different. In the limit of large unit cells ($CsPbI_3$ is the largest one considered here), the dominant contribution to the run time comes from the tasks that scale cubically with respect to the system size. These tasks include the construction of the Hamiltonian matrices and the diagonalization. As shown in Fig. 2, a converged SV calculation requires that essentially all unoccupied bands are included for solving the full problem. In this light, SV does not offer any advantage over the NP approach. In contrast, to converge the SVLO(p) calculation, it is sufficient to use a significantly smaller basis with $N_{\rm occ} = 228$, $N_{\rm LO} = 496$, and $N_{\rm unocc} \sim 0$ (see Table II). Taking into account the spin degrees of freedom, the size of the Hamiltonian matrix in the SV step is ∼1500. As discussed above, diagonalization is also required in the FV step, where the dimension of the SR Hamiltonian is ∼3800. This step is therefore the most computationally intensive in this example. Compared to the NP calculation, we find that total time spent on the FV and SV steps is reduced by a factor of 3.6. Finally, the inclusion of $p_{1/2}$-type LOs increases $N_{\rm LO}$ to 736 and thus also slightly increases the size of the SV diagonalization problem.

E. Bi_2Te_3

Bi_2Te_3 is a topological insulator with a single Dirac cone at Γ [51,52]. It is characterized by strong SOC effects, shifting the fundamental band gap from Γ to an off-symmetry point in the mirror plane of the first Brillouin zone that is displayed in the bottom panel of Fig. 4. The positions of the VBM and CBM are highly sensitive to the structure and

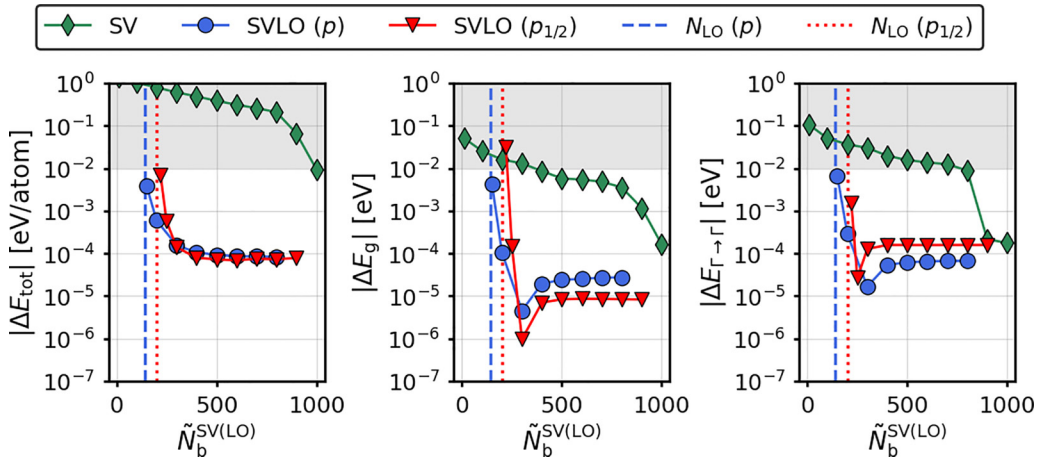

FIG. 6. Convergence behavior of the total energy, energy gap, and energy difference between the highest VB and the lowest CB at Γ with respect to the number of second-variational basis functions $\tilde{N}_b^{SV(LO)}$ for Bi_2Te_3.

the choice of the exchange-correlation functional; thus, there are controversial results present in the literature. Reference [53] presents an overview of this diversity, which increases when more accurate methods, such as the *GW* approximation, are applied [54,55]. All these aspects together make Bi_2Te_3 computationally challenging.

Bi_2Te_3 crystallizes in a rhombohedral structure with *R*-3*m* symmetry, shown in the top panel of Fig. 4. It consists of five layers, with alternating Te and Bi sheets, repeated along the z direction. There are two chemically inequivalent Te sites.

Including SOC, the band structure undergoes significant changes that are further enhanced when Dirac-type LOs are added [56,57] (top and middle panels of Fig. 5). A relevant difference is observed at Γ, where the valence band (VB) and the CB obtained from SOC calculations show a hump as a consequence of the band-inversion characteristic of this material [51,53]. Different from similar topological insulators, the hump is well preserved in spinor *GW* calculations, which include the off-diagonal elements of the self-energy, even though the band dispersion is strongly altered [55]. SR calculations lead to a direct band gap of 0.25 eV at Γ (Table III). By adding SOC but no Dirac-type LOs, it reduces to 0.10 eV and is located at point $B = (0.67, 0.58, 0.58)$, which appears sixfold in the BZ. Our results are comparable to those of Refs. [31,57]. In the former, a direct band gap of 0.13 eV at (0.667, 0.571, 0.571) was measured, while in the latter, a value of 0.11 eV was computed, but different from our result, it was reported to be indirect. However, the VBM and CBM are very close to each other, located at (0.652, 0.579, 0.579) and (0.663, 0.568, 0.568), respectively. One may assign these differences to the use of different $\boldsymbol{k}$ grids and crystal structures (here, we use $a = 10.44$ Å and $\theta = 24.27°$ [47], while Refs. [31,57] use an experimental structure with $a = 10.48$ Å and $\theta = 24.16°$).

By adding four $p_{1/2}$-type LOs for each species, i.e., a total of 60 basis functions (Table II), the gap reduces to 0.03 eV and becomes indirect. In the bottom panel of Fig. 5, we observe that the VB is lowered at B and raised at $D = (0.52, 0.35, 0.35)$, where the VBM is now located. The CB is not altered at B but is lowered at $C = (0.65, 0.54, 0.54)$, which is the approximate location of the CBM (the resolution is limited by the $48 \times 48 \times 48$ $\boldsymbol{k}$ mesh). Points C and D are sixfold degenerate. D is located between Γ and $A = (0.64, 0.43, 0.43)$, which lies on the path between Z and U. C and B are close to $Z \to F$. Larson [56] and Huang and Kaviany [57] obtained gaps of 0.05 and 0.07 eV, respectively, with $p_{1/2}$-type LOs. The locations of the band extrema slightly differ between those works and ours, with ours being in better agreement with that of Larson [56].

As is evident from Fig. 6, for Bi_2Te_3, our method has clear advantages over the conventional SV method, which reaches the target precision for the total energy only with basically all available FV KS states (about ∼1000; see Table II), while the SVLO method requires a basis-set size comparable to the number of LO basis functions (141 for the p set and 201 for the $p_{1/2}$ set). The SVLO method converges in either case within a precision of 10^{-4} eV/atom. Like for the other materials, the electronic structure obtained by SV converges faster than the total energy, but the convergence is still not comparable to that of the SVLO method. To obtain an energy gap within a precision of 10^{-2} eV, the SV method requires about two times the number of basis functions (without including the occupied states); to obtain $E_{\Gamma\to\Gamma}$ with the same precision, the basis size needs to be further doubled. The band gap converges to a precision of $\sim 10^{-5}$ eV, while the SV method cannot go lower than 10^{-4} eV.

V. DISCUSSION AND CONCLUSIONS

In this work, we introduced an approach called the SVLO method to treat spin-orbit coupling in DFT calculations efficiently. It allows us to obtain rapid convergence and highly precise results, e.g., band energies within the order of 10^{-4} eV or even better. SOC splittings and total energies within a precision of 10^{-2} eV and 10^{-2} eV/atom, respectively, can actually be obtained with a number of basis functions that is comparable to the number of occupied states plus a set of LOs. Its efficiency is due to the fact that SOC effects mainly come from regions around the atomic nuclei where atomiclike

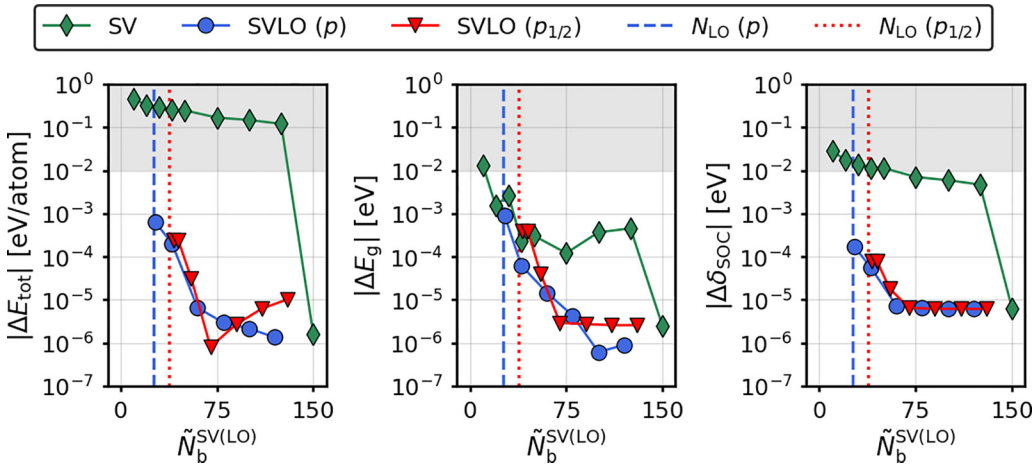

FIG. 7. Same as Fig. 2 for Xe, but for only one $\boldsymbol{k}$ point.

functions play a major role in describing them. We demonstrated this method with examples of very different materials. The use of the SVLO method is most efficient when SOC effects are strong. In these cases, we also observed significant contributions of $p_{1/2}$ LOs. Obviously, the overall gain of our method becomes more pronounced the bigger the system is. In summary, by providing a method that allows for reliable and efficient calculations of SOC, our work contributes to obtaining highly accurate electronic properties at the DFT level.

All input and output files are available from NOMAD [41,58].

ACKNOWLEDGMENTS

This work was supported by the German Research Foundation within the priority program SPP2196, "Perovskite Semiconductors" (project 424709454), and the CRC HIOS (project 182087777, B11). Partial support from the European Union's Horizon 2020 research and innovation program under Grant Agreement No. 951786 (NOMAD CoE) is appreciated. A.G. acknowledges funding provided by the European Regional Development Fund via the Central Finance and Contracting Agency of the Republic of Latvia under Grant Agreement No. 1.1.1.5/21/A/004.

APPENDIX

In the examples discussed above, the SV method often converges to worse precision than the SVLO method. This may appear counterintuitive since the two methods should be equivalent if the SV basis includes all available FV KS states. The reason for the seeming discrepancy comes from the fact that the LAPW basis-set size may be different at different $\boldsymbol{k}$ points, depending on their symmetry. In contrast, in the SV method, the size of the basis is controlled by an input parameter and limited by the number of available FV KS orbitals. In our implementation, the same number is considered for all $\boldsymbol{k}$ points. In Fig. 7, we show, for the example of Xe, that when carrying out the SVLO calculation with a single $\boldsymbol{k}$ point, the two methods reach the same precision (of the order of 10^{-6} eV) for all analyzed properties. In this case, all KS orbitals can be used as basis functions in the SV method. We emphasize, however, that the inclusion of all KS states is not efficient and thus is not desirable anyway.

[1] M. Marsili, A. Molina-Sánchez, M. Palummo, D. Sangalli, and A. Marini, Spinorial formulation of the *GW*-BSE equations and spin properties of excitons in two-dimensional transition metal dichalcogenides, Phys. Rev. B **103**, 155152 (2021).

[2] D. Y. Qiu, F. H. da Jornada, and S. G. Louie, Screening and many-body effects in two-dimensional crystals: Monolayer MoS_2, Phys. Rev. B **93**, 235435 (2016).

[3] F. Caruso, M. Schebek, Y. Pan, C. Vona, and C. Draxl, Chirality of valley excitons in monolayer transition-metal dichalcogenides, J. Phys. Chem. Lett. **13**, 5894 (2022).

[4] C. L. Kane and E. J. Mele, Quantum spin Hall effect in graphene, Phys. Rev. Lett. **95**, 226801 (2005).

[5] Y. Yao, F. Ye, X.-L. Qi, S.-C. Zhang, and Z. Fang, Spin-orbit gap of graphene: First-principles calculations, Phys. Rev. B **75**, 041401(R) (2007).

[6] M. Gmitra, S. Konschuh, C. Ertler, C. Ambrosch-Draxl, and J. Fabian, Band-structure topologies of graphene: Spin-orbit coupling effects from first principles, Phys. Rev. B **80**, 235431 (2009).

[7] J. Even, L. Pedesseau, J.-M. Jancu, and C. Katan, Importance of spin–orbit coupling in hybrid organic/inorganic perovskites for photovoltaic applications, J. Phys. Chem. Lett. **4**, 2999 (2013).

[8] E. van Lenthe, J. G. Snijders, and E. J. Baerends, The zero–order regular approximation for relativistic effects: The effect of spin–orbit coupling in closed shell molecules, J. Chem. Phys. **105**, 6505 (1996).

[9] M. J. T. Oliveira and X. Gonze, Spin–orbit effects in the bismuth atom and dimer: Tight-binding and density functional theory comparison, J. Phys. B **46**, 095101 (2013).

[10] A. Gulans and C. Draxl, Influence of spin-orbit coupling on chemical bonding, arXiv:2204.02751.

[11] A. D. Corso, *Ab initio* phonon dispersions of transition and noble metals: Effects of the exchange and correlation functional, J. Phys.: Condens. Matter **25**, 145401 (2013).

[12] C. Ming, H. Wang, D. West, S. Zhang, and Y.-Y. Sun, Defect tolerance in $CsPbI_3$: Reconstruction of the potential energy landscape and band degeneracy in spin–orbit coupling, J. Mater. Chem. A **10**, 3018 (2022).

[13] H. Eschrig, M. Richter, and I. Opahle, Relativistic solid state calculations, in *Relativistic Electronic Structure Theory*, edited by P. Schwerdtfeger, Theoretical and Computational Chemistry, Vol. 14 (Elsevier, Auckland, 2004), pp. 723–776.

[14] R. Zhao, Y. Zhang, Y. Xiao, and W. Liu, Exact two-component relativistic energy band theory and application, J. Chem. Phys. **144**, 044105 (2016).

[15] W. P. Huhn and V. Blum, One-hundred-three compound band-structure benchmark of post-self-consistent spin-orbit coupling treatments in density functional theory, Phys. Rev. Mater. **1**, 033803 (2017).

[16] M. Kadek, M. Repisky, and K. Ruud, All-electron fully relativistic Kohn-Sham theory for solids based on the Dirac-Coulomb Hamiltonian and Gaussian-type functions, Phys. Rev. B **99**, 205103 (2019).

[17] D. A. Rehn, J. M. Wills, T. E. Battelle, and A. E. Mattsson, Dirac's equation and its implications for density functional theory based calculations of materials containing heavy elements, Phys. Rev. B **101**, 085114 (2020).

[18] R. Zhao, V. W.-Z. Yu, K. Zhang, Y. Xiao, Y. Zhang, and V. Blum, Quasi-four-component method with numeric atom-centered orbitals for relativistic density functional simulations of molecules and solids, Phys. Rev. B **103**, 245144 (2021).

[19] M. Kadek, B. Wang, M. Joosten, W.-C. Chiu, F. Mairesse, M. Repisky, K. Ruud, and A. Bansil, Band structures and $\mathbb{z}_2$ invariants of two-dimensional transition metal dichalcogenide monolayers from fully relativistic Dirac-Kohn-Sham theory using gaussian-type orbitals, Phys. Rev. Mater. **7**, 064001 (2023).

[20] M. Schlipf and F. Gygi, Optimization algorithm for the generation of ONCV pseudopotentials, Comput. Phys. Commun. **196**, 36 (2015).

[21] A. Gulans, S. Kontur, C. Meisenbichler, D. Nabok, P. Pavone, S. Rigamonti, S. Sagmeister, U. Werner, and C. Draxl, Exciting: A full-potential all-electron package implementing density-functional theory and many-body perturbation theory, J. Phys.: Condens. Matter **26**, 363202 (2014).

[22] P. Blaha, K. Schwarz, P. Sorantin, and S. Trickey, Full-potential, linearized augmented plane wave programs for crystalline systems, Comput. Phys. Commun. **59**, 399 (1990).

[23] S. Blügel and G. Bihlmayer, An all-electron full-potential linearised augmented-plane wave (FP-LAPW) code, NIC Ser. **31**, 85 (2006).

[24] ELK, an all-electron full-potential linearised augmented-plane wave (LAPW) code, http://elk.sourceforge.net/.

[25] D. J. Singh, *Planewaves, Pseudopotentials and the LAPW Method* (Springer US, New York, 1994).

[26] D. D. Koelling and B. N. Harmon, A technique for relativistic spin-polarised calculations, J. Phys. C **10**, 3107 (1977).

[27] E. van Lenthe, E. J. Baerends, and J. G. Snijders, Relativistic regular two-component Hamiltonians, J. Chem. Phys. **99**, 4597 (1993).

[28] E. van Lenthe, E. J. Baerends, and J. G. Snijders, Relativistic total energy using regular approximations, J. Chem. Phys. **101**, 9783 (1994).

[29] T. L. Loucks, Relativistic electronic structure in crystals. I. Theory, Phys. Rev. **139**, A1333 (1965).

[30] A. L. Kutepov, Elimination of the linearization error in APW/LAPW basis set: Dirac-Kohn-Sham equations, Phys. Rev. B **103**, 165101 (2021).

[31] T. J. Scheidemantel, C. Ambrosch-Draxl, T. Thonhauser, J. V. Badding, and J. O. Sofo, Transport coefficients from first-principles calculations, Phys. Rev. B **68**, 125210 (2003).

[32] C. Vona, D. Nabok, and C. Draxl, Electronic structure of (organic-)inorganic metal halide perovskites: The dilemma of choosing the right functional, Adv. Theor. Simul. **5**, 2100496 (2022).

[33] L. Nordström, J. M. Wills, P. H. Andersson, P. Söderlind, and O. Eriksson, Spin-orbit coupling in the actinide elements: A critical evaluation of theoretical equilibrium volumes, Phys. Rev. B **63**, 035103 (2000).

[34] J. Kuneš, P. Novák, R. Schmid, P. Blaha, and K. Schwarz, Electronic structure of fcc Th: Spin-orbit calculation with $6p_{1/2}$ local orbital extension, Phys. Rev. B **64**, 153102 (2001).

[35] G. Michalicek, M. Betzinger, C. Friedrich, and S. Blügel, Elimination of the linearization error and improved basis-set convergence within the FLAPW method, Comput. Phys. Commun. **184**, 2670 (2013).

[36] D. Nabok, A. Gulans, and C. Draxl, Accurate all-electron G_0W_0 quasiparticle energies employing the full-potential augmented plane-wave method, Phys. Rev. B **94**, 035118 (2016).

[37] D. Zavickis, K. Kacars, J. Cīmurs, and A. Gulans, Adaptively compressed exchange in the linearized augmented plane wave formalism, Phys. Rev. B **106**, 165101 (2022).

[38] D. Singh, Ground-state properties of lanthanum: Treatment of extended-core states, Phys. Rev. B **43**, 6388 (1991).

[39] J. P. Perdew, K. Burke, and M. Ernzerhof, Generalized gradient approximation made simple, Phys. Rev. Lett. **77**, 3865 (1996).

[40] J. P. Perdew, K. Burke, and M. Ernzerhof, Erratum: Generalized gradient approximation made simple [Phys. Rev. Lett. **77**, 3865 (1996)], Phys. Rev. Lett. **78**, 1396(E) (1997).

[41] C. Vona, S. Lubeck, H. Kleine, A. Gulans, and C. Draxl, 2023, NOMAD, https://dx.doi.org/10.17172/NOMAD/2023.06.06-1.

[42] R. W. G. Wyckoff, *Crystal Structures*, 2nd ed. (Interscience, New York, 1963).

[43] N. Ashcroft and N. Mermin, *Solid State Physics* (Cengage Learning, Boston, 2011).

[44] T. Böker, R. Severin, A. Müller, C. Janowitz, R. Manzke, D. Voß, P. Krüger, A. Mazur, and J. Pollmann, Band structure of MoS_2, $MoSe_2$, and α-$MoTe_2$: Angle-resolved photoelectron spectroscopy and *ab initio* calculations, Phys. Rev. B **64**, 235305 (2001).

[45] B. Palosz, The structure of PbI_2 polytypes 2H and 4H: A study of the 2H-4H transition, J. Phys.: Condens. Matter **2**, 5285 (1990).

[46] R. J. Sutton, M. R. Filip, A. A. Haghighirad, N. Sakai, B. Wenger, F. Giustino, and H. J. Snaith, Cubic or orthorhombic? Revealing the crystal structure of metastable black-phase $CsPbI_3$ by theory and experiment, ACS Energy Lett. **3**, 1787 (2018).

[47] V. R. Akshay, M. V. Suneesh, and M. Vasundhara, Tailoring thermoelectric properties through structure and morphology in chemically synthesized n-type bismuth telluride nanostructures, Inorg. Chem. **56**, 6264 (2017).

[48] E. Cappelluti, R. Roldán, J. A. Silva-Guillén, P. Ordejón, and F. Guinea, Tight-binding model and direct-gap/indirect-gap transition in single-layer and multilayer MoS_2, Phys. Rev. B **88**, 075409 (2013).

[49] M. Pisarra, C. Díaz, and F. Martín, Theoretical study of structural and electronic properties of 2*H*-phase transition metal dichalcogenides, Phys. Rev. B **103**, 195416 (2021).

[50] Z. Yao, W. Zhao, and S. F. Liu, Stability of the $CsPbI_3$ perovskite: From fundamentals to improvements, J. Mater. Chem. A **9**, 11124 (2021).

[51] H. Zhang, C.-X. Liu, X.-L. Qi, X. Dai, Z. Fang, and S.-C. Zhang, Topological insulators in Bi_2Se_3, Bi_2Te_3 and Sb_2Te_3 with a single Dirac cone on the surface, Nat. Phys. **5**, 438 (2009).

[52] Y. L. Chen, J. G. Analytis, J.-H. Chu, Z. K. Liu, S.-K. Mo, X. L. Qi, H. J. Zhang, D. H. Lu, X. Dai, Z. Fang, S. C. Zhang, I. R. Fisher, Z. Hussain, and Z.-X. Shen, Experimental realization of a three-dimensional topological insulator, Bi_2Te_3, Science **325**, 178 (2009).

[53] T. Fang, X. Li, C. Hu, Q. Zhang, J. Yang, W. Zhang, X. Zhao, D. J. Singh, and T. Zhu, Complex band structures and lattice dynamics of Bi_2Te_3-based compounds and solid solutions, Adv. Funct. Mater. **29**, 1900677 (2019).

[54] E. Kioupakis, M. L. Tiago, and S. G. Louie, Quasiparticle electronic structure of bismuth telluride in the *GW* approximation, Phys. Rev. B **82**, 245203 (2010).

[55] I. Aguilera, C. Friedrich, G. Bihlmayer, and S. Blügel, *GW* study of topological insulators Bi_2Se_3, Bi_2Te_3, and Sb_2Te_3: Beyond the perturbative one-shot approach, Phys. Rev. B **88**, 045206 (2013).

[56] P. Larson, Effect of $p_{1/2}$ corrections in the electronic structure of Bi_2Te_3 compounds, Phys. Rev. B **68**, 155121 (2003).

[57] B.-L. Huang and M. Kaviany, *Ab initio* and molecular dynamics predictions for electron and phonon transport in bismuth telluride, Phys. Rev. B **77**, 125209 (2008).

[58] C. Draxl and M. Scheffler, The NOMAD laboratory: From data sharing to artificial intelligence, J. Phys.: Mater. **2**, 036001 (2019).